Exploring the tricritical nature and unconventional magnetoresistance in $EuCd_2P_2$: An in-depth study of complex material characteristics

Azizur Rahman,[1,*] Majeed Ur Rehman,[2,3,*,†] Yue Zhang,[4] Weisheng Zhao,[4] Jianlin Wang,[5,6] Zheng Chen,[7,‡] Zahir Muhammad,[4,§] and Lei Zhang[7,‖]

[1]*Department of Physics, University of Science and Technology of China, Hefei 230026, China*
[2]*Songshan Lake Materials Laboratory, Dongguan, Guangdong 523808, China*
[3]*Institute of Physics, Chinese Academy of Sciences, Beijing 100190, China*
[4]*Hefei Innovation Research Institute, School of Integrated Circuit Science and Engineering, Beihang University, Hefei 230013, China*
[5]*Hefei National Research Center for Physical Sciences at the Microscale, University of Science and Technology of China, Hefei 230026, China*
[6]*Anhui Laboratory of Advanced Photon Science and Technology, University of Science and Technology of China, Hefei 230026, China*
[7]*Anhui Key Laboratory of Low-Energy Quantum Materials and Devices, High Magnetic Field Laboratory, Hefei Institutes of Physical Science, Chinese Academy of Sciences, Hefei 230031, China*

(Received 26 February 2024; revised 13 June 2024; accepted 25 July 2024; published 7 August 2024)

$EuCd_2P_2$, a layered phosphide crystal, exhibits a nonconventional magnetoresistive trend that deviates from typical material behavior. This unique characteristic prompts further intriguing and complex investigation. Herein, we utilize critical exponent analysis, angle-resolved photoemission spectroscopy (ARPES), and density functional theory to uncover physical insights into $EuCd_2P_2$. Magnetization analysis reveals a persistent ferromagnetic phase above the antiferromagnetic phase, extending to higher temperatures at high magnetic fields. Critical behavior analysis of $H \parallel ab$ reveals critical exponents $\beta = 0.2432(2)$, $\gamma = 0.883(2)$, and $\delta = 4.63(1)$, aligning with a three-dimensional tricritical mean-field model coupled with long-range interaction ($\sigma = 1.53$). The H-T phase diagram establishes a tricritical point ($H = 620$ Oe, $T = 18.3$ K), signifying diverse spin interactions and magnetic phases. Temperature-dependent ARPES discloses significant modifications in the electronic band spectrum of $EuCd_2P_2$ during the spin ordering transitions, characterized by a substantial band gap alteration and valence band splitting. Remarkably, the semiconducting properties of $EuCd_2P_2$ remain unaffected throughout these transitions. First-principles simulations unveil a near-degenerate coexistence of layer-antiferromagnetic and -ferromagnetic phases, significant valence band modifications in CdP due to distinct proximity effects induced by the Eu lattice's spin-magnetic moments, and the half-metallic phases in ferromagnetic $EuCd_2P_2$ crystals. These findings advance our understanding of magnetic and electronic properties in $EuCd_2P_2$.

DOI: 10.1103/PhysRevB.110.064407

I. INTRODUCTION

The temperature-dependent resistivity $\rho(T)$ is a typical approach for identifying phase transitions in novel materials. It shows changes in slope at magnetic transitions, and the heat capacity anomaly is linked to the derivative $d\rho/dT$. According to Fisher-Langer theory, this behavior arises from critical fluctuations that enhance quasiparticle scattering [1]. However, in specific metallic magnets, $\rho(T)$ behaves in a way beyond a simple slope change, making them more interesting and unusual. For instance, recent studies identified resistivity peaks near the Néel temperature T_N in antiferromagnetic (AFM) europium compounds (EuM_2C_2, with M = In, Cd and C = Sb, As, P) [2–7]. In these materials, the type of magnetic order significantly influences the electronic structure and low-energy topology [8–10]. Furthermore, the near degeneracy of multiple magnetic states makes them experimentally accessible [11,12], offering the potential to create highly responsive electronic states. One of these AFM compounds, $EuCd_2P_2$, has drawn considerable attention due to its remarkably unique $\rho(T)$ properties [5]. It exhibits a resistivity peak with a 100-fold increase well above the T_N of 11.5 K. Modest magnetic fields can suppress the maximum resistivity value observed at 18 K (above T_N), resulting in substantial negative magnetoresistance. The emergence of colossal magnetoresistance (CMR) in $EuCd_2P_2$ has been attributed to various factors, including magnetic fluctuations [5], the magnetic Berezinskii-Kosterlitz-Thouless transition [13,14], and ferromagnetic (FM) cluster formation [15]. Nevertheless, the exact microscopic factors behind the resistivity peak remain a topic of ongoing debate.

Addressing the intrinsic magnetization within $EuCd_2P_2$, our study aims to deepen the understanding of the interplay between magnetic ordering and electronic properties, which will shed light on both microscopic and macroscopic aspects.

*These authors contributed equally to this work.
†Contact author: majeedqau@live.com
‡Contact author: chenzheng@hmfl.ac.cn
§Contact author: zahir@mail.ustc.edu.cn
‖Contact author: zhanglei@hmfl.ac.cn

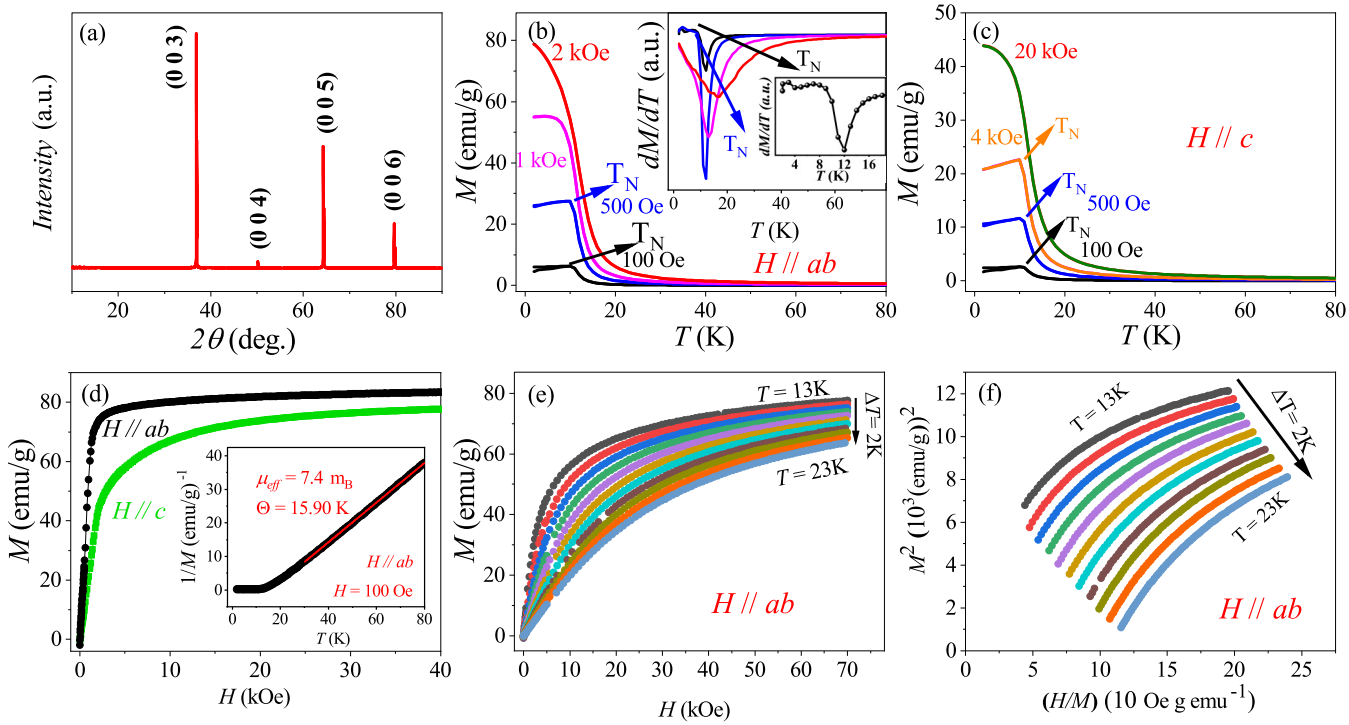

FIG. 1. (a) Single-crystal XRD pattern of $EuCd_2P_2$ at room temperature. The observed sharp $(00l)$ peaks imply the high quality of the $EuCd_2P_2$ single crystal. (b) Temperature dependence of magnetization $M(T)$ for $H \parallel ab$. The inset shows the derivative magnetization dM/dT vs T of ZFC curves for magnetic field $H \parallel ab$, and the zoomed-in region in the low-temperature region shows the AFM features. The arrows show the AFM transition at low temperature. (c) $M(T)$ curves for $H \parallel c$. The arrows show the AFM transition at low temperature (discussed in the text). (d) The field-dependent magnetization $[M(H)]$ curves at 5 K for both $H \parallel ab$ and $H \parallel c$. The inset shows the reciprocal of the susceptibility $\chi^{-1}(T)$ with applied field $H = 100$ Oe for $H \parallel ab$. (e) Initial isothermal magnetization curves around T_C for $H \parallel ab$. (f) Arrott plot of M^2 vs H/M around T_C for $H \parallel ab$.

Previous research has explored the influence of magnetic ordering on electronic properties [16]. However, the mechanisms underlying the complex shifts in the electronic band structure and the role of spin configuration changes across resistivity maxima remain less understood. This study seeks to unravel these intricate questions by investigating whether changes in the electronic band structure alone are responsible for the observed phenomena or whether alterations in the spin configuration also contribute to the CMR mechanism. Furthermore, the nature of the FM spin ordering, whether it constitutes a short-range proximity effect or a well-established long-range phase, remains an open question.

Our approach involves a comprehensive investigation employing critical behavior spin analysis to unveil the nature, range, and universality class of the spin-ordered phase near the magnetic transition. Angle-resolved photoemission spectroscopy (ARPES) analysis is utilized to monitor electronic band spectrum variations around spin configuration shifts, which provides valuable insights into the simultaneous variation of electronic and spin characteristics. Furthermore, density functional theory (DFT) analysis is employed to elucidate the intricate details of the mechanisms driving these variations within $EuCd_2P_2$ [17–20].

II. RESULTS AND DISCUSSION

Single crystals of $EuCd_2P_2$ were synthesized using the flux technique [5]. The experimental details and characterization are described in the Supplemental Material [21]. These resulting crystals exhibit a triangular and platelike morphology. $EuCd_2P_2$ possesses a trigonal lattice within the space group $P\bar{3}m1$, featuring alternating Eu and Cd layers [5]. These layers consist of triangular networks comprising either edge-shared EuP_6 octahedra or CdP_4 tetrahedra. The c-axis x-ray diffraction pattern of a grown $EuCd_2P_2$ crystal is illustrated in Fig. 1(a), revealing distinct $(00l)$ diffraction lines. The presence of sharp peaks in the diffraction pattern signifies the exceptional quality of the grown crystals.

$EuCd_2P_2$ is verified to be an A-type AFM material. For the AFM features, a peak at 11 K can apparently be observed in temperature-dependent magnetization $M(T)$ curves with external magnetic field H applied along both the c axis and ab plane [see Figs. 1(b) and 1(c)]. The significantly large magnetic moment observed for $H \parallel ab$ compared to $H \parallel c$ is consistent with early work that indicated the easy-plane anisotropy in $EuCd_2P_2$ [5]. The distinctive AFM peak in the ab plane disappears at $H = 0.2$ T in the $M(T)$ curve. Conversely, for $H \parallel c$, $EuCd_2P_2$ maintains its AFM spin configuration until $H = 0.4$ T. However, above this field, the $M(T)$ curves at low temperatures for $H \parallel c$ also become flat below T_N, as shown in Fig. 1(c), confirming a field-induced AFM-FM transition. Consequently, the magnetic ground state reflected from our $M(T)$ curves is AFM, consistent with prior observations. However, close examination of the $M(T)$ curves reveals the sharp decrease immediately above T_N, demonstrating the coexistence of AFM and FM features. The dM/dT

curves are shown in the inset of Fig. 1(b) to confirm the coexistence AFM and FM phases. A low-temperature peak (corresponding to T_N) is accompanied by a valley (a typical FM feature). The broad peak in dM/dT vanishes, and FM characteristic minima move towards higher temperature at high fields, agreeing with the $M(T)$ curves. Figure 1(d) illustrates the isothermal magnetization of $EuCd_2P_2$ at $T =$ 5 K with magnetic field orientations $H \parallel ab$ and $H \parallel c$. This observation reveals an obvious easy-plane magnetization in $EuCd_2P_2$, consistent with the trends observed in the $M(T)$ curves. Figure 1(d) suggests a fixed Eu^{2+} oxidation state ($4f^7$ configuration) since the low-temperature saturation magnetization ($7.6\mu_B$) and high-temperature effective moment ($8.1\mu_B$) are consistent with theoretically predicted values for Eu^{2+} ($7\mu_B$ and $8\mu_B$, respectively). The $\chi^{-1}(T)$ curves fitted by the Curie-Weiss law [$\chi = C/(T - \Theta)$] show positive, but considerably lower, Curie-Weiss temperatures Θ of the same order as T_N for magnetic fields H applied in the ab plane or along the c axis [see the inset of Fig. 1(d)]. The positivity of Θ implies FM magnetic fluctuations above T_N, while its smallness compared to the fluctuation temperature supports competing interactions of either sign.

To obtain insight into the paramagnetic-to-ferromagnetic (PM-FM) transition of $EuCd_2P_2$, we performed isothermal $M(H)$ measurements spanning a temperature range of 13 to 23 K for $H \parallel ab$, as shown in Fig. 1(e). Figure 1(f) displays the Arrott plot [22,23], revealing nonlinear behavior across all curves, even in high fields. This observation suggests that the mean-field model is not suitable for $EuCd_2P_2$. Nevertheless, the concave downward curvature indicates that the PM-FM transition in $EuCd_2P_2$ is a second-order transition. Consequently, a self-consistent method is employed to establish a modified Arrott plot for determining T_C and the critical exponents β and γ, utilizing the Arrott-Noaks equation of state:

$$(H/M)^{1/\gamma} = a\varepsilon + bM^{1/\beta}, \tag{1}$$

where $\varepsilon = (T - T_C)/T_C$ is the reduced temperature, while a and b are constants. Using Eq. (1), we examine the isothermal data using three-dimensional (3D) models, including the 3D Heisenberg model ($\beta = 0.365$, $\gamma = 1.386$), 3D XY model ($\beta = 0.346$, $\gamma = 1.316$), 3D Ising model ($\beta = 0.325$, $\gamma = 1.240$), and tricritical mean-field model ($\beta = 0.25$, $\gamma = 1.0$; see the Supplemental Material for the details [21]). The findings in Figs. S2(a)–S2(d) demonstrate that quasiparallel straight lines were generated [21]. However, none intersected at the origin, suggesting that the utilized models cannot describe $EuCd_2P_2$ accurately. The normalized slope (NS), $\mathrm{NS} = S(T)/S(T_C)$, where S is the slope of a single line of $M^{1/\beta}$ and $(H/M)^{1/\gamma}$, is employed to determine the optimal model for $EuCd_2P_2$. The tricritical mean-field model that displays the smallest deviation from "1" among all the models analyzed is deemed the most suitable [Fig. 2(a)], although precise fitting of critical exponents is essential.

The iterative method was used to find proper values of β and γ [23]. Starting with values from the tricritical mean-field model plotted by linear extrapolation to intercepts with axes $M^{1/\beta}$ and $(H/M)^{1/\gamma}$, a new set of β and γ is obtained by fitting data using the following equations:

$$M_S(T) = M_0(-\varepsilon)^{\beta}, \quad \varepsilon < 0, \quad T < T_C, \tag{2}$$

$$\chi_0^{-1}(T) = (h_0/M_0)\varepsilon^{\gamma}, \quad \varepsilon > 0, \quad T > T_C, \tag{3}$$

$$M = DH^{1/\delta}, \quad \varepsilon = 0, \quad T = T_C. \tag{4}$$

The newly obtained values utilizing Eqs. (2) and (3) are used to reconstruct the modified Arrott plot, and the procedure is repeated until stable values are obtained. The final modified Arrott plots are shown in Fig. 2(b). Figure 2(c) shows the final $M_S(T)$ and $\chi_0^{-1}(T)$ with fitting curves, which yield the critical exponents $\beta = 0.2432(2)$ with $T_C = 17.38(2)$ K and $\gamma = 0.883(2)$ with $T_C = 17.45(9)$ K.

Figure 2(d) displays the isothermal magnetization $M(H)$ at a critical temperature of $T_C = 18$ K; the inset shows the same plot on a log-log scale. Using Eq. (4), we deduce the third critical exponent $\delta = 4.63(1)$. Additionally, we can calculate δ by applying the Widom scaling relation, which states that the critical exponents β, γ, and δ are interrelated as follows:

$$\delta = 1 + \frac{\gamma}{\beta}. \tag{5}$$

Using the β and γ values from the modified Arrott plot in Eq. (5), we get $\delta = 4.46(3)$, close to the value from a critical isotherm analysis.

In a homogeneous magnet, the exchange distance $J(r)$ determines the universality class of the magnetic phase transition. According to renormalization group theory, the interaction decays with distance r as $J(r) \approx r^{-(d+\sigma)}$, where d is the spatial dimensionality and σ is a positive constant. The spin interaction has a long or short range depending on $\sigma < 2$ and $\sigma > 2$, and it predicts the susceptibility exponent obtained using a renormalization group theory technique as follows [24]:

$$\gamma = 1 + \frac{4}{d}\left(\frac{n+2}{n+8}\right)\Delta\sigma + \frac{8(n+2)(n-4)}{d^2(n+8)^2} \times \left[1 + \frac{2G\left(\frac{d}{2}\right)(7n+20)}{(n-4)(n+8)}\right]\Delta\sigma^2, \tag{6}$$

where $\Delta\sigma = (\sigma - \frac{d}{2})$, $G(\frac{d}{2}) = 3 - \frac{1}{4}(\frac{d}{2})^2$, and n is the spin dimensionality. We employed an approach similar to that in Ref. [25] to establish the range of interaction σ, as well as the dimensionality of the lattice d and spin n. For particular values of $\{d : n\}$, the parameter in the expression above is changed to get a result close to the experimentally noted $\gamma = 1.326$. The obtained value is then used to calculate the other exponents using the following formulas: $\nu = \gamma/\sigma$, $\alpha = 2 - \nu d$, $\beta = (2 - \alpha - \gamma)/2$, and $\delta = 1 + \gamma/\beta$. We find that $\{d : n\} = 3{:}3$ and $\sigma = 1.21$ yield exponents γ consistent with experimental values. The critical exponent $\alpha = 2 - \nu d \approx 0$ aligns with the predicted $\alpha = 0$ in the mean-field model [26]. This calculation shows that the spin interaction in $EuCd_2P_2$ is long range, decaying as $J(r) \approx r^{-(4.21)}$.

The scaling hypothesis can verify the critical exponents. Using the renormalized magnetization $m \equiv \varepsilon^{-\beta}M(H, \varepsilon)$ and the renormalized field $h \equiv \varepsilon^{-(\beta+\gamma)}$, the scaling equation in the asymptotic critical region is given as follows:

$$m = f_{\pm}(h), \tag{7}$$

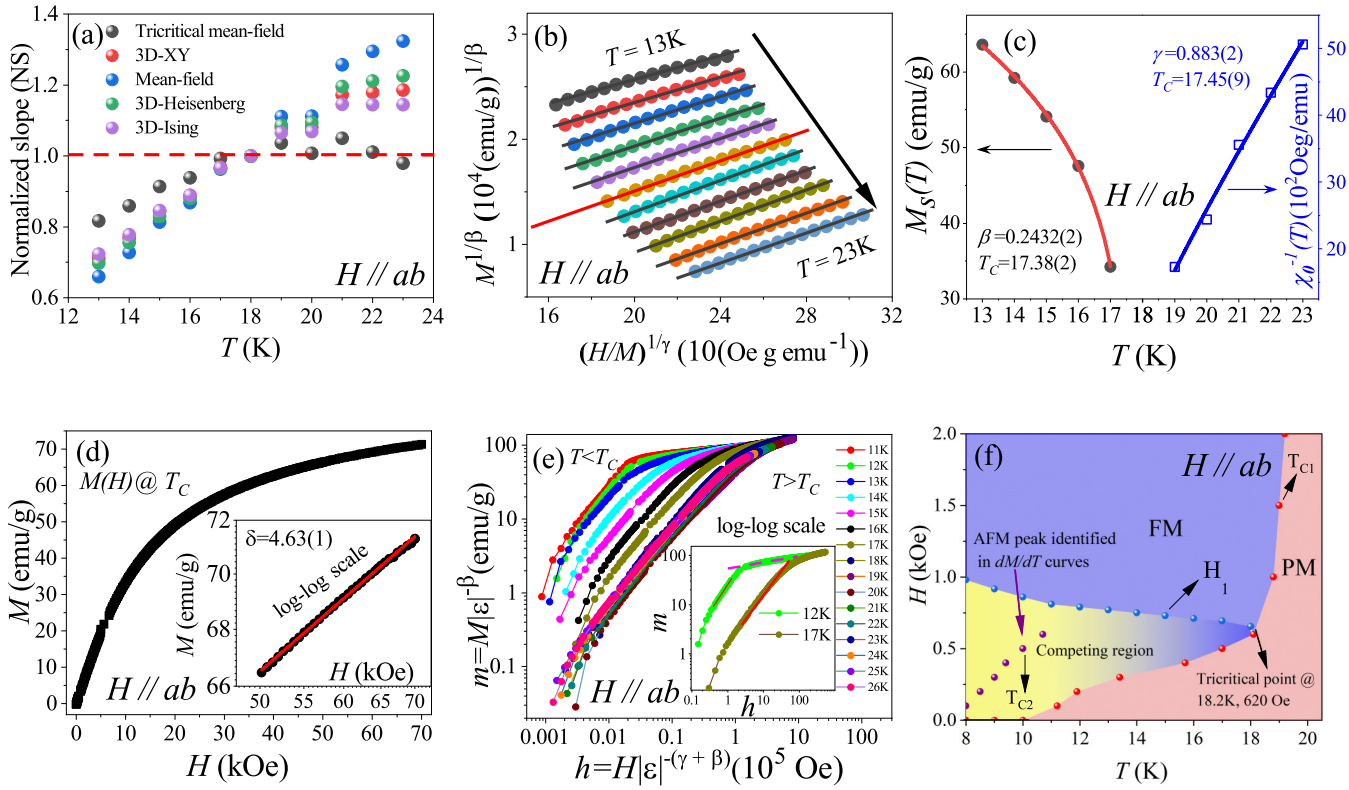

FIG. 2. (a) Normalized slope (NS) as a function of temperature, defined as NS $= S(T)/S(T_C)$ for $H \parallel ab$. (b) Final modified Arrott plot of $M^{1/\beta}$ vs $(H/M)^{1/\gamma}$ with $\beta = 0.2432(2)$ and $\gamma = 0.883(2)$ for $H \parallel ab$. (c) Temperature dependence of the spontaneous magnetization $M_S(T)$ (left) and the inverse initial susceptibility $\chi_0^{-1}(T)$ (right) with solid fitting curves for $EuCd_2P_2$ with $H \parallel ab$. (d) Magnetic isotherm at $T_C =$ 18 K for $H \parallel ab$. The inset shows the same isotherm in log-log scale. The red line shows the linear fitting. (e) Scaling plots of renormalized m vs renormalized h around T_C for $M(H)$ at typical temperatures in log-log scale (the inset shows the same plot for selected temperatures). (f) Detailed H-T phase diagram around the tricritical point of single-crystal $EuCd_2P_2$ for $H \parallel ab$. T_{C1}, T_{C2}, and H_1 are discussed in the text.

where f_+ for $T > T_c$ and f_- for $T < T_c$ are the regular functions. Using Eq. (7), $M(H)$ curves are scaled into $m(h)$ with the critical exponents, forming two distinct universal branches for $T > T_C$ and $T < T_C$, respectively [27]. Figure 2(e) depicts the m vs h relationship in the high-field region ($H > H_S$). The $m(h)$ curves adhere to the universality principle and bifurcate into two distinct branches above and below T_C for $H > H_S$. Consequently, the obtained critical exponents are self-consistent and reliable. However, the $m(h)$ curves below T_C are slightly dispersed in the low-field region. The Γ-shaped m vs h/m curves at selected temperatures below T_C in the inset of Fig. 2(e) indicate distinguishable regions or phases. The inflection point is marked as H_1 on each curve. The multiple phases of single-crystal $EuCd_2P_2$ with $H \parallel ab$ are concisely depicted in the phase diagram in Fig. 2(f). Phase boundaries are determined using magnetization data and universality scaling analysis. T_{C1} is derived from the minima of dM/dT, T_{C2} is ascertained from the peak in dM/dT, and H_1 is identified at the inflection point on $m(h)$. The diagram illustrates the coexistence of AFM and FM phases, shifting to higher temperatures with increased magnetic fields. A tricritical point (TCP) is precisely located at the intersection of the AFM, FM, and PM phases.

Table I presents a comparative analysis of the critical exponents associated with $EuCd_2P_2$ and theoretical models. The critical exponents observed in $EuCd_2P_2$ are in close prox-

TABLE I. Comparison of critical exponents of $EuCd_2P_2$ in different theoretical models.

Composition	Refs.	Technique	β	γ	δ
$EuCd_2P_2$	This work	Modified Arrott plot	0.2432(2)	0.883(2)	4.63(1)
Tricritical mean field	[28]	Theory	0.25	1.0	5
3D Heisenberg	[29,30]	Theory	0.365	1.386	4.8
3D XY	[29,30]	Theory	0.345	1.316	4.81
3D Ising	[29,30]	Theory	0.325	1.24	4.82
Two-dimensional Ising	[31]	Theory	0.125	1.75	15
Mean field	[32]	Theory	0.5	1.0	3.0

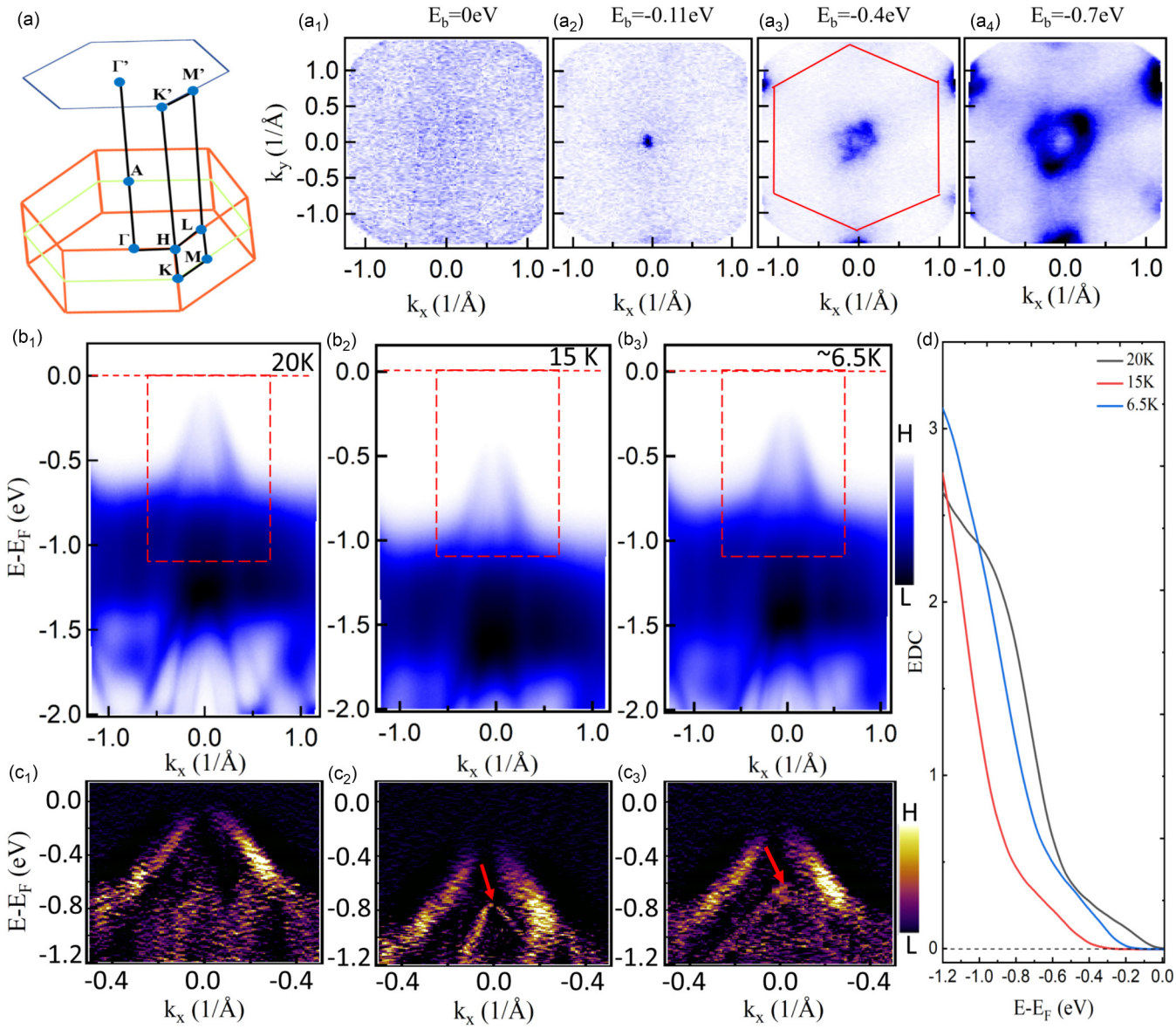

FIG. 3. ARPES measurements on $EuCd_2P_2$ single crystals. (a) Schematic of the bulk and corresponding surface BZ for $EuCd_2P_2$. (a_1)–(a_4) Fermi surface maps at various binding energies measured at 20 K using 100 eV photon energy. (b_1)–(b_3) Band dispersion along Γ-*K* and (c_1)–(c_3) the corresponding second derivatives measured at 20, 15, and 6.5 K, respectively. The second derivatives were taken from the red dashed boxes in (b_1)–(b_3). The red arrows in (c_1)–(c_3) show the corresponding split. (d) Temperature evolution of the EDCs spectra. The band dispersion was measured at 50 eV photon energy.

imity to those characterizing a tricritical mean-field model. This model is particularly relevant in systems exhibiting a tricritical phenomenon, characterized by the simultaneous presence of multiple phases. The coexistence of diverse phases suggests the complex interplay of numerous interactions and couplings in the system. Moreover, the intricate equilibrium in the system makes its properties highly susceptible to external influences, including pressure, applied fields, doping, etc. The degeneracy of magnetic phases was previously documented in numerous EuM_2C_2 compounds. With DFT simulations, it was ascertained that the low-energy electronic structure and topology of these EuM_2C_2 compounds undergo substantial modifications as a consequence of the inherent nature of magnetic ordering [8–10]. A parallel expectation is posited for $EuCd_2P_2$, wherein its electronic features are envisaged to exhibit heightened sensitivity to external stimuli.

The electronic characteristics of $EuCd_2P_2$ single crystals were investigated through an ARPES experiment, as illustrated in Fig. 3. Fermi surface (FS) mapping at 20 K, utilizing a photon energy of 100 eV reveals the absence of electron pockets proximate to the Fermi level (FL) at 0 eV binding energy, as depicted in Fig. 3(a_1). However, an observable spectral weight is discerned at the FS when moving to lower binding energies, approximately −0.11 eV, corresponding to the valence bands near the Γ point, thus contributing to the

FS [see the FS maps in Fig. 3(a_2)]. Further scrutiny of the FS at lower binding energies provides additional insights. The FS maps disclose the presence of six Fermi pockets along the edges and a circular Fermi pocket at the center of the first Brillouin zone (BZ) around the Γ point. This configuration collectively forms a hexagonal FS, as evidenced in Figs. 3(a_3) and 3(a_4).

The investigation of the temperature-dependent evolution of the band structure in $EuCd_2P_2$ centered around the magnetic transition temperature is presented in Figs. 3(b_1)–3(b_3). The depicted energy versus moment cut along the high-symmetry Γ-*K* points illustrates the band structure alongside their respective second derivatives as a function of temperature near the transition temperature. In Figs. 3(b_1) and 3(c_1), the band structure is characterized by a valence band maximum (VBM) positioned approximately 100 meV below the FL, revealing a minimal gap at 20 K. However, with a decrease in temperature to 15 K [which is evident in Fig. 3(b_2)], the VBM undergoes a notable shift to approximately 320 meV below the FL. Examining Figs. 3(b_2) and 3(c_2), we can discern that the gap within the band structure widens, and a very pronounced magnetic band splitting becomes evident in the proximity of the FM phase transition. Additionally, as shown in the $M(T)$ data illustrated in Figs. 1(b) and 1(c), distinct phases emerge, characterized by a plateau in the temperature behavior (PM phase), a sudden surge around 15 K (FM phase), and a peak at roughly 11 K (AFM phase). Consequently, we conducted band dispersion measurements below 11 K. Examination of the band dispersion at 6.5 K [see Figs. 3(b_3) and 3(c_3)] reveals a shift of the VBM back to approximately 140 meV below the FL. This provides evidence of electronic band spectrum modification during the AFM transition. However, the magnetic band splitting manifestation persists and is minimally affected by the VBM shift in the AFM transition.

The second derivative analysis reveals the splitting of the VBM at the Γ point, a phenomenon that intensifies with decreasing temperature and correlates with magnetic ordering. The temperature-dependent evolution of the energy distribution curve (EDC) spectra, as depicted in Fig. 3(d), elucidates the electronic characteristics of $EuCd_2P_2$. At 20 K (in the PM phase), the EDC spectra indicate that the spectral weight is in close proximity to the FL. In contrast, at 15 K (around the FM transition), the spectral weight is noticeably distant from the FL. Notably, at lower temperatures, specifically at 6.5 K (around the AFM transition), the spectral weight converges towards the FL [see Fig. 3(d)]. However, across the assessed temperature spectrum, the $EuCd_2P_2$ persists in a semiconductor state, a characteristic distinct from the metallic phase recently identified in ARPES measurements of $EuCd_2P_2$ near the FM transition [16]. The metallic FM phase typically manifests in a substance characterized by a mixed valence, facilitating an FM double-exchange interaction and a structural Jahn-Teller distortion [33–36]. These factors collaboratively induce a phase transition from a PM insulator to an FM metal. The emergence of the FM metallic phase in the referenced study [16] could potentially be attributed to the presence of mixed valence Eu^{2+}/Eu^{3+} in the $EuCd_2P_2$ crystals used. Nevertheless, our analysis of magnetization data has effectively eliminated the possibility of the coexistence of mixed valence Eu^{2+}/Eu^{3+}. Therefore, the ARPES measurement in this work substantiates that $EuCd_2P_2$ undergoes a significant band spectrum alteration while retaining its semiconductor character. The absence of a mixed valence (confirmed in magnetization measurement) further reinforces the logical and unequivocal nature of this phenomenon. We also incorporated a momentum distribution curve to elucidate the temperature-dependent evolution of band features in the $EuCd_2P_2$ sample (see Fig. S3 in the Supplemental Material [21]). These ARPES results offer a comprehensive depiction of the temperature-dependent evolution of the band structure, underscoring their alignment with the magnetic ordering in $EuCd_2P_2$. However, elucidating how spin ordering transitions exert influence on the electronic band structure requires comprehensive explanation. Therefore, to address this issue effectively, it is essential to establish the microscopic origins of magnetization in $EuCd_2P_2$.

To identify the correct magnetic ground state of $EuCd_2P_2$, we conducted spin-polarized calculations, considering the spin configurations in the FM state and interlayer AFM (A-AFM) states, AFM1 and AFM2 (see Fig. S4 in the Supplemental Material [21]). In the FM configuration, both intralayer and interlayer spin interactions are set to be FM. Conversely, in the A-AFM configuration, intralayer interactions are FM, while interlayer interactions assume an AFM arrangement. In the AFM1 state, the spin magnetic moments are ordered antiferromagnetically within each Eu layer and ferromagnetically between the Eu layers. In the AFM2 state, the spins are ordered antiferromagnetically both within and between the Eu layers. Our spin-polarized first-principles calculations unveil that the A-AFM state serves as the ground magnetic state for $EuCd_2P_2$, exhibiting energy lower by approximately 0.5 meV per unit cell compared to the FM state. This slight energy barrier suggests the potential coexistence of FM and A-AFM configurations in the $EuCd_2P_2$ crystal. The FM state can be stabilized by applying a minor magnetic field. Before we delve into the details of how spin arrangements affect electronic properties in the $EuCd_2P_2$ crystal, it is crucial to first explain the microscopic origin of magnetization. This is closely linked to changes in the band structure resulting from alterations in the spin arrangement in the $EuCd_2P_2$ crystal. The magnetization in the $EuCd_2P_2$ crystal primarily arises from the interaction of Eu atoms. The size of the spin magnetic moment on each Eu atom is $6.94\mu_B$ in both FM and A-AFM states, corresponding to an effective magnetic moment μ_{eff} of $7.86\mu_B$. This is in good agreement with the estimates obtained from the experiments. The crystal structure of $EuCd_2P_2$ can be conceptualized as CdP layers sandwiched between Eu layers [see Fig. 4(a)]. Consequently, the magnetic moment induced in CdP layers is influenced by the spin arrangement of the Eu layers. For instance, in the A-AFM arrangement, the spin moments induced in the sandwiched CdP(1) and CdP(2) layers are opposite [see Fig. 4(a)], whereas in the FM configuration, the spin moments in both the CdP(1) and CdP(2) layers are parallel, as shown in Fig. 4(f). Similarly, the spin magnetic moments induced in the CdP(1) and CdP(2) layers are parallel to the Eu(1) and Eu(2) layers, respectively [Fig. 4(a)] in the case of A-AFM. However, in the FM case, the induced moments are antiparallel to the Eu(1) and Eu(2) layers. Although the induced

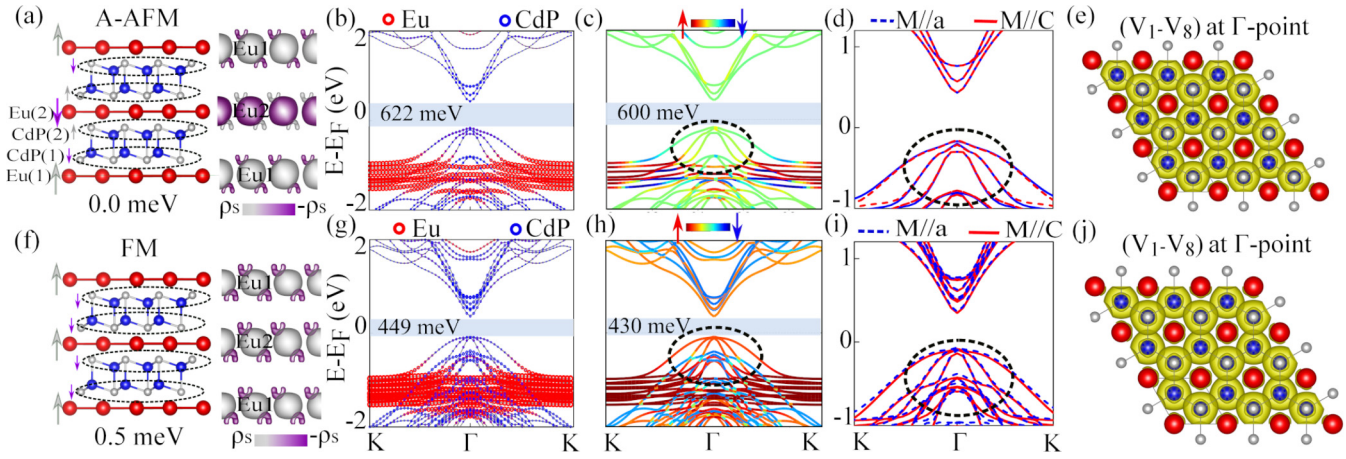

FIG. 4. (a)–(e) and (f)–(j) correspond to A-AFM and FM states of the $EuCd_2P_2$ crystal. (a) Side view of the magnetic crystal structure ($1 \times 1 \times 2$) of $EuCd_2P_2$ in the A-AFM state, with vertical arrows representing spin magnetic moments. (b) Spin-polarized electronic band structures of $EuCd_2P_2$ in the A-AFM state, highlighting contributions from Eu and CdP with red and blue circles, respectively. (c) S_z-resolved band structure of the $EuCd_2P_2$ crystal in the A-AFM state (SOC included). (d) SOC-included band structure of the $EuCd_2P_2$ crystal in the A-AFM state for the cases $M \parallel a$ (blue dashed curves) and $M \parallel c$ (red solid curves). (e) Band-decomposed charge density profile at the Γ point for the top eight valence bands (V_1–V_8) in the A-AFM state. (f)–(j) are the same as (a)–(e), but for the FM state.

magnetic moments in Cd2P2 are small (around $0.024\mu_B$), they significantly impact electronic states near the Fermi level [Figs. 4(b) and 4(g)].

Our atomic-resolved electronic band structure reveals that the electronic bands around the Fermi level primarily originate from the P states, which partially hybridize with the Cd and Eu states [Figs. 4(c) and 4(h)]. Although the Eu states are situated away from the Fermi surface, they exert control over the bands around the Fermi level by inducing different spin magnetic moments in the CdP layers (as discussed above). This phenomenon is indeed the reason behind the pronounced modification of the valence bands near the Fermi level when changing from the A-AFM to FM arrangement. The band structure alteration is evident in Fig. 4. The electronic band structure undergoes significant changes during the A-AFM to FM transition in the $EuCd_2P_2$ system. Specifically, within the magnetic phase transition from A-AFM to FM, several key observations emerge. First, the global band gap remains present but experiences a reduction in size from 600 to 400 meV, affirming the semiconducting nature of $EuCd_2P_2$ as observed in our experiments. Second, the valence bands demonstrate spin polarization, as illustrated in Fig. 4(h). Third, there is variation in the splitting size within the valence bands, as depicted in Figs. 4(d) and 4(i). These collective observations underscore the significant impact on electronic properties when the $EuCd_2P_2$ system undergoes a magnetic phase transition from A-AFM to FM. Importantly, these findings align with the experimental data obtained through ARPES, offering a comprehensive understanding of the electronic behavior during the magnetic transition.

To further confirm that the modifications in the band structure of $EuCd_2P_2$, when changing from the A-AFM state to FM states, are linked to the induced spin magnetic moments in CdP sandwiched layers, we calculated the spin-resolved band structure in the presence of spin-orbit coupling (SOC). We observe that states belonging to the CdP layers get split when the interlayer spin moments are ferromagnetically aligned, whereas spin splitting is not observed in the case of the A-AFM configuration. This once again confirms that the interlayer spin arrangement has a strong link to the magnetization induced in the CdP sandwiched layers. Interestingly, the S_z-resolved band structure reveals that a half-metallic phase in the FM states of $EuCd_2P_2$ can be probed through slight hole doping in the sample. This establishes that $EuCd_2P_2$ can exhibit half-metallic properties in its FM states. Additionally, we calculated the electronic band structures in A-AFM states by considering spin orientation along the in-plane and out-of-plane directions. The electronic band structure remains robust against spin orientation, completely consistent with our estimated small barrier of magnetic anisotropy energy (around 20/unit cell).

III. CONCLUSION

In conclusion, our intensive examination of the layered phosphide crystal $EuCd_2P_2$ has unraveled a dynamic interplay between magnetism and electronic spectrum characteristics. The material exhibits intricate magnetic phase transitions, changing from a PM to an FM state and eventually to an AFM state at low temperatures and fields. We identified the FM transition as second order, revealing long-range spin interactions with tricritical mean-field-like characteristic with critical exponents $\beta = 0.2432(2)$, $\gamma = 0.883(2)$, and $\delta = 4.63(1)$. Utilizing scaling analysis, we constructed a comprehensive H-T phase diagram, pinpointing a TCP ($H = 620$ Oe, $T = 18.3$ K), representing the convergence of multiple phases. The significance of our findings is underscored by ARPES measurements, which demonstrates the marked sensitivity of electronic states near the Fermi level to spin ordering. Substantial valence band splitting and a rigid shift manifest this sensitivity, shedding light on the impact of the spin ordering moment associated with Eu ($6.94\mu_B$/Eu). Despite these transitions, $EuCd_2P_2$ maintains its semiconductor attributes.

Our first-principles calculation revealed a direct link between the band structure alteration in $EuCd_2P_2$ and the induced spin magnetic moments in CdP sandwiched layers during the transition from the A-AFM state to FM states. Bands belonging to Cd2P2 layers exhibit splitting when interlayer spin moments are ferromagnetically aligned, in contrast to the A-AFM configuration, where no spin splitting occurs. The induced magnetic moments in CdP layers, influenced by the spin arrangement in the Eu layer, significantly impact electronic states near the Fermi level. Notably, FM states exhibit a half-metallic phase if slightly doped with hole carriers. Additionally, electronic band structures in A-AFM states display resilience against spin orientation changes. This thorough study clarifies the complex relationship between magnetism and electrical behavior in $EuCd_2P_2$, opening up new avenues for research into layered phosphide crystals and their potential applications.

ACKNOWLEDGMENTS

This work was supported by the National Natural Science Foundation of China (Grants No. 12350410367, No. 12250410238, No. 62150410438, No. 12374128, and No. 12074386), the Alliance of International Science Organizations (ANSO; Grants No. ANSO-VF-2022-03 and No. ANSO-VF-2024-03), the Basic Research Program of the Chinese Academy of Sciences Based on Major Scientific Infrastructures, China (Grant No. JZHKYPT-2021-08), the National Key R and D Program of China (Grants No. 2023YFA1610100 and No. 2019YFA0405600), and the Anhui Provincial Key R and D Program (Grant No. 202104a05020012). Part of this research used Beamline 03U of the Shanghai Synchrotron Radiation Facility, which is supported by the ME2 project under Contract No. 11227902 from the National Natural Science Foundation of China.

[1] M. E. Fisher and J. Langer, Resistive anomalies at magnetic critical points, Phys. Rev. Lett. **20**, 665 (1968).

[2] J.-Z. Ma, S. M. Nie, C. J. Yi, J. Jandke, T. Shang, M. Y. Yao, M. Naamneh, L. Q. Yan, Y. Sun, A. Chikina, V. N. Strocov, M. Medarde, M. Song, Y.-M. Xiong, G. Xu, W. Wulfhekel, J. Mesot, M. Reticcioli, C. Franchini, C. Mudry, M. Müller, Y. G. Shi, T. Qian, H. Ding, and M. Shi, Spin fluctuation induced Weyl semimetal state in the paramagnetic phase of $EuCd_2As_2$, Sci. Adv. **5**, eaaw4718 (2019).

[3] Y. Xu, L. Das, J. Z. Ma, C. J. Yi, S. M. Nie, Y. G. Shi, A. Tiwari, S. S. Tsirkin, T. Neupert, M. Medarde, M. Shi, J. Chang, and T. Shang, Unconventional transverse transport above and below the magnetic transition temperature in Weyl semimetal $EuCd_2As_2$, Phys. Rev. Lett. **126**, 076602 (2021).

[4] M. C. Rahn, J.-R. Soh, S. Francoual, L. Veiga, J. Strempfer, J. Mardegan, D. Y. Yan, Y. F. Guo, Y. G. Shi, and A. T. Boothroyd, Coupling of magnetic order and charge transport in the candidate Dirac semimetal $EuCd_2As_2$, Phys. Rev. B **97**, 214422 (2018).

[5] Z.-C. Wang, J. D. Rogers, X. Yao, R. Nichols, K. Atay, B. Xu, J. Franklin, I. Sochnikov, P. J. Ryan, D. Haskel, and F. Tafti, Colossal magnetoresistance without mixed valence in a layered phosphide crystal, Adv. Mater. **33**, 2005755 (2021).

[6] H. Su, B. Gong, W. Shi, H. Yang, H. Wang, W. Xia, Z. Yu, P.-J. Guo, J. Wang, L. Ding, L. Xu, X. Li, X. Wang, Z. Zou, N. Yu, Z. Zhu, Y. Chen, Z. Liu, K. Liu, G. Li, and Y. Guo, Magnetic exchange induced Weyl state in a semimetal $EuCd_2Sb_2$, APL Mater. **8**, 011109 (2020).

[7] Y. Zhang, K. Deng, X. Zhang, M. Wang, Y. Wang, C. Liu, J.-W. Mei, S. Kumar, E. F. Schwier, K. Shimada, C. Chen, and B. Shen, In-plane antiferromagnetic moments and magnetic polaron in the axion topological insulator candidate $EuIn_2As_2$, Phys. Rev. B **101**, 205126 (2020).

[8] Y. Xu, Z. Song, Z. Wang, H. Weng, and X. Dai, Higher-order topology of the axion insulator $EuIn_2As_2$, Phys. Rev. Lett. **122**, 256402 (2019).

[9] G. Hua, S. Nie, Z. Song, R. Yu, G. Xu, and K. Yao, Dirac semimetal in type-IV magnetic space groups, Phys. Rev. B **98**, 201116(R) (2018).

[10] J.-R. Soh, C. Donnerer, K. M. Hughes, E. Schierle, E. Weschke, D. Prabhakaran, and A. T. Boothroyd, Magnetic and electronic structure of the layered rare-earth pnictide $EuCd_2Sb_2$, Phys. Rev. B **98**, 064419 (2018).

[11] N. H. Jo, B. Kuthanazhi, Y. Wu, E. Timmons, T.-H. Kim, L. Zhou, L.-L. Wang, B. G. Ueland, A. Palasyuk, D. H. Ryan, R. J. McQueeney, K. Lee, B. Schrunk, A. A. Burkov, R. Prozorov, S. L. Bud'ko, A. Kaminski, and P. C. Canfield, Manipulating magnetism in the topological semimetal $EuCd_2Sb_2$, Phys. Rev. B **101**, 140402(R) (2020).

[12] N. H. Jo, Y. Wu, T. V. Trevisan, L.-L. Wang, K. Lee, B. Kuthanazhi, B. Schrunk, S. L. Bud'ko, P. C. Canfield, P. P. Orth, and A. Kaminski, Visualizing band selective enhancement of quasiparticle lifetime in a metallic ferromagnet, Nat. Commun. **12**, 7169 (2021).

[13] B. Flebus, Magnetoresistance driven by the magnetic Berezinskii-Kosterlitz-Thouless transition, Phys. Rev. B **104**, L020408 (2021).

[14] E. Heinrich, T. Posske, and B. Flebus, Topological magnetic phase transition in Eu-based A-type antiferromagnets, Phys. Rev. B **106**, 214402 (2022).

[15] V. Sunko, Y. Sun, M. Vranas, C. C. Homes, C. Lee, E. Donoway, Z.-C. Wang, S. Balguri, M. B. Mahendru, A. Ruiz, B. Gunn, R. Basak, S. Blanco-Canosa, E. Schierle, E. Weschke, F. Tafti, A. Frano, and J. Orenstein, Spin-carrier coupling induced ferromagnetism and giant resistivity peak in $EuCd_2P_2$, Phys. Rev. B **107**, 144404 (2023).

[16] H. Zhang, F. Du, X. Zheng, S. Luo, Y. Wu, H. Zheng, S. Cui, Z. Sun, Z. Liu, D. Shen, M. Smidman, Y. Song, M. Shi, Z. Zhong, C. Cao, H. Yuan, and Y. Liu, Electronic band reconstruction across the insulator-metal transition in colossally magnetoresistive $EuCd_2P_2$, Phys. Rev. B **108**, L241115 (2023).

[17] G. Kresse and J. Furthmüller, Efficient iterative schemes for *ab initio* total-energy calculations using a plane-wave basis set, Phys. Rev. B **54**, 11169 (1996).

[18] P. E. Blöchl, Projector augmented-wave method, Phys. Rev. B **50**, 17953 (1994).

[19] J. P. Perdew, K. Burke, and M. Ernzerhof, Generalized gradient approximation made simple, Phys. Rev. Lett. **77**, 3865 (1996).

[20] S. L. Dudarev, G. A. Botton, S. Y. Savrasov, C. J. Humphreys, and A. P. Sutton, Electron-energy-loss spectra and the structural stability of nickel oxide: An LSDA+ U study, Phys. Rev. B **57**, 1505 (1998).

[21] See Supplemental Material at http://link.aps.org/supplemental/10.1103/PhysRevB.110.064407 for the experimental and computational details, ARPES, and band calculation analysis.

[22] A. Rahman, M. U. Rehman, M. Yousaf, H. Zhao, K. Ruan, R. Dai, Z. Wang, L. Zhang, Z. Chen, and Z. Zhang, Magnetization-direction-tunable spin coupling in kagome magnet $LiMn_6Sn_6$, Mater. Today Phys. **35**, 101114 (2023).

[23] A. Rahman, M. U. Rehman, M. Kiani, H. Zhao, J. Wang, Y. Lu, K. Ruan, R. Dai, Z. Wang, L. Zhang, J. Wang, and Z. Zhang, Critical behavior and phase diagram of layered ferromagnetic $FeTa_3S_6$ single crystals, Phys. Rev. B **105**, 144413 (2022).

[24] H. Han, L. Zhang, D. Sapkota, N. Hao, L. Ling, H. Du, L. Pi, C. Zhang, D. G. Mandrus, and Y. Zhang, Tricritical point and phase diagram based on critical scaling in the monoaxial chiral helimagnet $Cr_{1/3}NbS_2$, Phys. Rev. B **96**, 094439 (2017).

[25] S. F. Fischer, S. N. Kaul, and H. Kronmüller, Critical magnetic properties of disordered polycrystalline $Cr_{75}Fe_{25}$ and $Cr_{70}Fe_{30}$ alloys, Phys. Rev. B **65**, 064443 (2002).

[26] Z. Du, A. Rahman, J. Song, J. Zhao, W. Liu, J. Fan, C. Ma, M. Ge, Y. Xiong, L. Pi, L. Zhang, and Y. Zhang, Field-induced anisotropic magnetic phase transitions and tricritical phenomena in $GdCr_6Ge_6$, Sci. China-Phys. Mech. Astron. **66**, 297511 (2023).

[27] A. Rahman, M. U. Rehman, H. Zhao, W. Liu, J. Wang, Y. Lu, K. Ruan, R. Dai, Z. Wang, X. Tao, L. Zhang, and Z. Zhang, Itinerant magnetism in the half-metallic Heusler compound Co_2HfSn: Evidence from critical behavior combined with first-principles calculations, Phys. Rev. B **103**, 094425 (2021).

[28] S. J. Poon and J. Durand, Critical phenomena and magnetic properties of an amorphous ferromagnet: Gadolinium-gold, Phys. Rev. B **16**, 316 (1977).

[29] B. Banerjee, On a generalised approach to first and second order magnetic transitions, Phys. Lett. **12**, 16 (1964).

[30] M. Campostrini, M. Hasenbusch, A. Pelissetto, P. Rossi, and E. Vicari, Critical exponents and equation of state of the three-dimensional Heisenberg universality class, Phys. Rev. B **65**, 144520 (2002).

[31] A. Rahman, M. U. Rehman, D. Zhang, M. Zhang, X. Wang, R. Dai, Z. Wang, X. Tao, L. Zhang, and Z. Zhang, Critical behavior in the half-metallic Heusler alloy Co_2TiSn, Phys. Rev. B **100**, 214419 (2019).

[32] H. E. Stanley, *Phase Transitions and Critical Phenomena* (Clarendon, Oxford, 1971).

[33] M. Subramanian, B. Toby, A. Ramirez, W. Marshall, A. Sleight, and G. Kwei, Colossal magnetoresistance without Mn^{3+}/Mn^{4+} double exchange in the stoichiometric pyrochlore $Tl_2Mn_2O_7$, Science **273**, 81 (1996).

[34] A. Ramirez, R. J. Cava, and J. Krajewski, Colossal magnetoresistance in Cr-based chalcogenide spinels, Nature (London) **386**, 156 (1997).

[35] J. Y. Chan, S. M. Kauzlarich, P. Klavins, R. N. Shelton, and D. J. Webb, Colossal magnetoresistance in the transition-metal Zintl compound $Eu_{14}MnSb_{11}$, Chem. Mater. **9**, 3132 (1997).

[36] I. R. Fisher, T. A. Wiener, S. L. Bud'ko, P. C. Canfield, J. Y. Chan, and S. M. Kauzlarich, Thermodynamic and transport properties of single-crystal $Yb_{14}MnSb_{11}$, Phys. Rev. B **59**, 13829 (1999).